

New Insights on the Role of Chloride During the Onset of Local Corrosion: TEM, APT, Surface Energy, and Morphological Instability

Xiao-xiang Yu,^{†,*} Ahmet Gulec,^{*} Katie Lutton Cwalina,^{**} John R. Scully,^{**} and Laurence D. Marks^{*}

The role of chloride in aqueous corrosion during local oxide destabilization as a precursor to breakdown is investigated by combining transmission electron microscopy, atom probe tomography, and density functional theory (DFT). The observations show that cube-cube epitaxy of rock-salt structure oxide initiates at the metal surface in the sodium sulfate electrolyte, which is not the "conventional" nickel oxide as a large number of solute Cr atoms are captured. The rock-salt oxide thin film roughens and a Cr-rich oxide with corundum structure grows out in chloride containing media. DFT calculations reveal the competitive chemisorption between hydroxide and chloride on hydroxylated NiO (111) and Cr₂O₃ (001) surfaces. The collective results relate the surface energy reduction to morphological instability and roughening due to chloride chemisorption in aqueous corrosion.

KEY WORDS: atom probe tomography, corrosion, chloride, density functional theory, transmission electron microscopy

INTRODUCTION

The presence of chloride ions in aqueous conditions is known to change the stability of the protective oxide film, in many cases leading to breakdown that may be either local or global and catastrophic.¹⁻⁴ The exact source of this is somewhat understood, but there are many uncertainties still being significant debated.⁵⁻⁶ In a recent work, the effect of competitive chemisorption of chloride on the hydroxylated surfaces of MgO (111), Al₂O₃ (001), and (100) was analyzed using density functional theory (DFT).⁷ The overall conclusion was that the chloride reduced the surface energy of the oxides, with significant differences depending on the crystallographic orientation of the oxide surfaces. These results indicate that morphological instability, which will become more likely when the surface energy is reduced, is the probable source or first stage of oxide breakdown processes leading to exposure of the metallic substrate. This is consistent with early work such as that of Hoar⁸ who suggested that chloride chemisorption would reduce the stabilizing surface energy driver, Sato⁹ who considered electrostriction as the destabilizing driver and surface energy as the stabilizing driver, and also Xu¹⁰ who considered oxide rupture and breakdown leading to pitting via a balance of field-induced stresses and surface energy. The crystallographic dependence is consistent with the adsorption/aggressive ion model,¹¹⁻¹⁵ while changes in the apparent wetting of the oxide and grain-boundary grooving are consistent with models that propose grain boundary attack.^{8,10,13,16-20} Rather than one model alone being the correct interpretation of the effect of chloride ions, the theoretical calculations suggest that chloride has simultaneously multiple

effects, so the different models present in the literature are all somewhat correct, albeit each alone is incomplete.

While theoretical calculations can provide guidance to understand processes, they rarely involve all the parameters present in real systems—they are computational experiments that probe some of the elementary processes taking place. For a real alloy, the oxides will be much more complex, with nanoscale grains, grain boundaries, and multiple surfaces of different orientations. Hence, experiments are required to test whether the computational experiments are representative. In this paper, we investigate experimentally the effect of chloride ions in solution, examining the microstructure and composition of the oxide formed on Ni-Cr films using transmission electron microscopy (TEM) and atom probe tomography (APT), with a few additional DFT calculations on the effect of chloride on the surface energy of hydroxylated NiO (111) and Cr₂O₃ (001) surfaces. The experimental results are overall consistent with the prior theoretical analysis of the effects of chloride⁷ and show a critical factor in the oxide thin film destabilization leading to breakdown is competitive chloride chemisorption in aqueous corrosion.

EXPERIMENTAL AND COMPUTATIONAL METHODS

2.1 | Electrochemical Corrosion Studies

Ni-22%Cr (wt%) alloys were prepared in an arc furnace, and the electrochemical testing was conducted in sodium chloride and sodium sulfate solutions acidified to pH 4 to study the oxide growth in different environments, as shown in Table 1.

Submitted for publication: July 25, 2018. Revised and accepted: January 17, 2019. Preprint available online: January 17, 2019, <https://doi.org/10.5006/2991>.

[†] Corresponding author. E-mail: yuxx07@gmail.com.

^{*} Department of Materials Science and Engineering, Northwestern University, Evanston, IL 60208.

^{**} Department of Materials Science & Engineering, University of Virginia, PO Box 400745, 395 McCormick Road, Charlottesville, VA 22904.

Table 1. Electrolytes Used for Electrochemical Experiments

| pH | NonCl ⁻ Electrolyte | Cl ⁻ Electrolyte |
|----|--|--|
| 4 | 0.1 M Na ₂ SO ₄ + 0.0001 M K ₂ S ₂ O ₈ | 0.1 M NaCl + 0.0001 M HCl + H ₂ O ₂ |

From the bulk samples, TEM and APT samples were prepared as described below. These were then corroded in an identical manner as planar electrodes. For the electrochemical treatments, chloride conditions were used with 200 mL of a 0.1 M NaCl solution adjusted with 0.1 mM HCl to pH 4 and 1 μ L to 5 μ L of H₂O₂ (30%) was used as an oxidizing agent. Alternatively, in chloride-free solutions persulfate was added to produce an identical oxidizing potential. The use of redox species in lieu of a conventional three-electrode cell configuration was chosen because the small geometry of the TEM foil and atom probe tips prohibited their use in such a set-up. Even attaching a lead to a potentiostat for enabling potentiostatic polarization was not possible. As such, we placed the fine samples into a solution containing the redox species which imposed an open circuit potential around +0.2 V vs. a saturated calomel reference electrode (SCE), a potential within the passive region on Ni-22%Cr. Polarization to 0.2 V_{SCE} revealed repassivation in both solutions with a slightly higher passive current density and sharp current spikes in Cl⁻. Verification of nearly identical oxides obtained from this method compared to a conventional potentiostat polarization method was achieved by electrochemical impedance. In both cases, specimens were oxidized for 10,000 s. The reduction of K₂S₂O₈ yields SO₄²⁻, which is identical to the soluble Na₂SO₄ chemical species produced during potentiostatic polarization experiments. Similarly, H₂O₂ reduction produces H₂O and OH⁻. The use of sulfate solutions provides a less-corrosive environment that will enable passivity characterization over a broader range of conditions than the chloride solution.

2.2 | Transmission Electron Microscopy

TEM samples were prepared using a low-speed saw (Buehler, IsoMet[†]) to cut the bulk sample into thin slices (~0.7 mm), then mechanical thinned to less than 100 μ m using sandpapers. From the thin slices, several 3 mm disks were cut with a disk cutter (South Bay Technology, Model 360[†]) and dimpled (VCR group, Inc., D500i[†]) to the thickness of 10 μ m to 20 μ m. Finally, the samples were ion milled at 3 keV to 6 keV (Gatan precision ion polishing system, Model 691[†]) until a small hole appeared, followed by (final) low energy and low angle argon ion milling (Fischione Model 1040 NanoMill[†]) at 500 eV to remove the amorphous and implanted layers. After preparation, the samples were electrochemically treated (as described above). Samples were examined using JEOL 2100F[†], and aberration-corrected JEOL ARM200CF[†] scanning transmission electron microscope (STEM) operated at 200 keV. Electron energy loss spectroscopy (EELS) analysis was performed with a Gatan GIF system attached to the microscope.

2.3 | Atom Probe Tomography

The samples for APT were prepared by a standard electropolishing procedures: 0.5 mm \times 0.5 mm \times 2 cm alloys bars were electropolished in an electrolyte of 10% (vol%) perchloric

acid in acetic acid using 12 V to 20 V DC for prethinning. Then 2% (vol%) perchloric acid in a butoxyethanol electrolyte and 12 V to 15 V DC were used for the final thinning. After preparation, the samples were treated using the electrochemical process detailed above.

A CAMECA Local Electrode Atom Probe 4000XSi[†] with an ultrafast detector capability was used for APT experiments. Picosecond pulses of ultraviolet laser light were utilized to evaporate individual atoms at a pulse repetition rate of 250 kHz, a laser pulse energy of 20 pJ per pulse and an average detection rate of 0.005 ions per pulse. The specimen tip temperature was maintained at 25 K. Data analyses were performed on the 3D reconstructions of specimens utilizing the program IVAS 3.6.1[†].

It is known²¹⁻²³ that the stoichiometry of oxide in laser-assisted APT depends upon the laser pulse energy and base temperature, and only approaches the correct value as the laser energy is reduced toward zero and the temperature is decreased to the absolute zero Kelvin. To calibrate the data, a tip of pure nickel was oxidized in lab air at 200°C for 20 min. Nickel oxide thin film with the stoichiometry of 1:1 for the Ni to O was assumed to form on the nickel tip surface. The APT experimental conditions (temperature, laser pulse energy, etc.) were kept the same as the corrosion samples. From Supplemental Figure 1, this sample indicates that the detection efficiency of oxygen at the same laser pulse energy and temperature is 2/3. All the APT data shown later has been corrected for the detection efficiency of the oxygen.

2.4 | Density Functional Calculations

Spin-polarized DFT calculations were performed using the Vienna *Ab initio* Simulation Package[†] (VASP)²⁴⁻²⁶ and the all-electron augmented plane wave + local orbitals WIEN2K[†] code.²⁷ The structures used were those previously calculated for the MgO (111) and Al₂O₃ (001) surface,⁷ with for the starting point the lattice adjusted and the appropriate antiferromagnetic ordering incorporated.

For nickel oxide (111), VASP calculations were performed using the projector augmented wave (PAW) method²⁸ and evaluated the exchange-correlation energy using the Perdew-Burke-Ernzerhoff (PBE) functional²⁹ with a plane wave cutoff is 550 eV, a conventional plus Hubbard *U* correction (SGGA + *U*) was used following the approach of Dudarev, et al.³⁰ Based upon calibration calculations, for nickel in nickel oxide a value of $U_{\text{eff}} = 5.3$ eV for the correlated Ni 3D orbitals was used in all simulations leading to reasonable values for the band gap, formation energies, magnetic moment, and bulk modulus.³¹ A $9 \times 9 \times 1$ k mesh was used for the k points sampling using the Monkhorst-Pack scheme³² during structural relaxation until the forces on each ion were less than 0.01 eV/Å, and a $12 \times 12 \times 2$ k mesh was used in the electronic structure calculation with a convergence of 10^{-5} eV for the total energy.

For Cr₂O₃ (001) and (100) WIEN2K²⁷ calculations were performed with the onsite-exact exchange/hybrid approach³³⁻³⁵ applied to the d-orbitals of Cr atoms with 25% of exact exchange. For the (001) surface the long dimension normal to the surface was 4.477 nm, for (001) 3.984 nm, in both cases with approximately 1/3 of the cell vacuum. Final atomic positions are included as crystallographic information files (CIF) in the Supplemental Material. All calculations were performed with antiferromagnetic inversion symmetry of the full surface slab, which avoids potential artifacts due to dipole fields. The PBE functional²⁹ was used for the potential and the SCAN meta-GGA³⁶ for the final exchange-correlation energies. Technical parameters were RMTs of 0.55, 1.2, 1.75, and 1.85 for H, O, Cr,

[†] Trade name.

and Cl atoms, with an RKMAX of 2.75, a GMAX of 20, over-sampling of the interstitial exchange-correlation potential of 1.8 and within the muffin tins up to spherical harmonics of order 18. All atom positions except those fixed by symmetry were relaxed to an accuracy of 1 mRyd/au or better using a parallel quasi-Newton algorithm.³⁷

RESULTS

We will describe the results separately, with and without chloride, combining the electron microscopy, atom probe, and DFT calculations. We will reserve extensive discussion of the significance to the discussion.

3.1 | Experimental Results Without Chloride

After corrosion in the sodium sulfate electrolyte, the oxide with rock-salt structure grows out and forms thin flakes on the Ni-Cr samples, as shown in Figures 1(a) and (b). The cube-cube epitaxy growth relationship by two face-centered cubic (fcc) structures is shown in the diffraction patterns of Figure 1(c) in which the extra spots appear with the same symmetry and orientation as the main spots of fcc Ni-Cr but have a smaller lattice spacing.

The reason that we do not claim the rock-salt structure oxide is the “conventional” nickel oxide is that a large amount of

Cr was captured in the rock-salt structure as APT results show in Figure 2(a). Why this occurs is discussed in more detail elsewhere,³⁸ and we will only provide a brief explanation here. When an oxide forms on an alloy, there will be a thermodynamic driving force to form the equilibrium oxides, but this can only occur if the oxidation fronts are moving slowly enough for the full interchange of atoms (particularly cations) to achieve this. If the interfaces are moving fast on the scale of atomic diffusion, unusual nonequilibrium phases are formed. We call this scientific framework “Nonequilibrium Solute Capture,” and it appears to be general for many alloys during aqueous corrosion as well as during high-temperature oxidation.³⁸

From the APT data, the outermost $\text{Ni}_{1-x}\text{Cr}_x\text{O}_y$ layer has about 14 at% to 25 at% Cr doping. The reported maximum solubility of Cr in NiO is only 1 at% at 950°C;³⁹ here the concentration of Cr in NiO is much larger than the thermodynamic equilibrium value. For completeness, we note that the compositional results shown in Figure 2 were reproduced for three samples, both with and without chloride.

The STEM-EELS measurements of composition and electronic structure of Cr captured in rock-salt were also used for cross-checking with APT data. Composition profile by EELS in Figure 3(a) also shows a large amount of Cr in the rock-salt structure after oxidation in sodium sulfate. Furthermore, Figure 3(b) shows L_3 edge of Cr in alloys is positioned at 575 eV

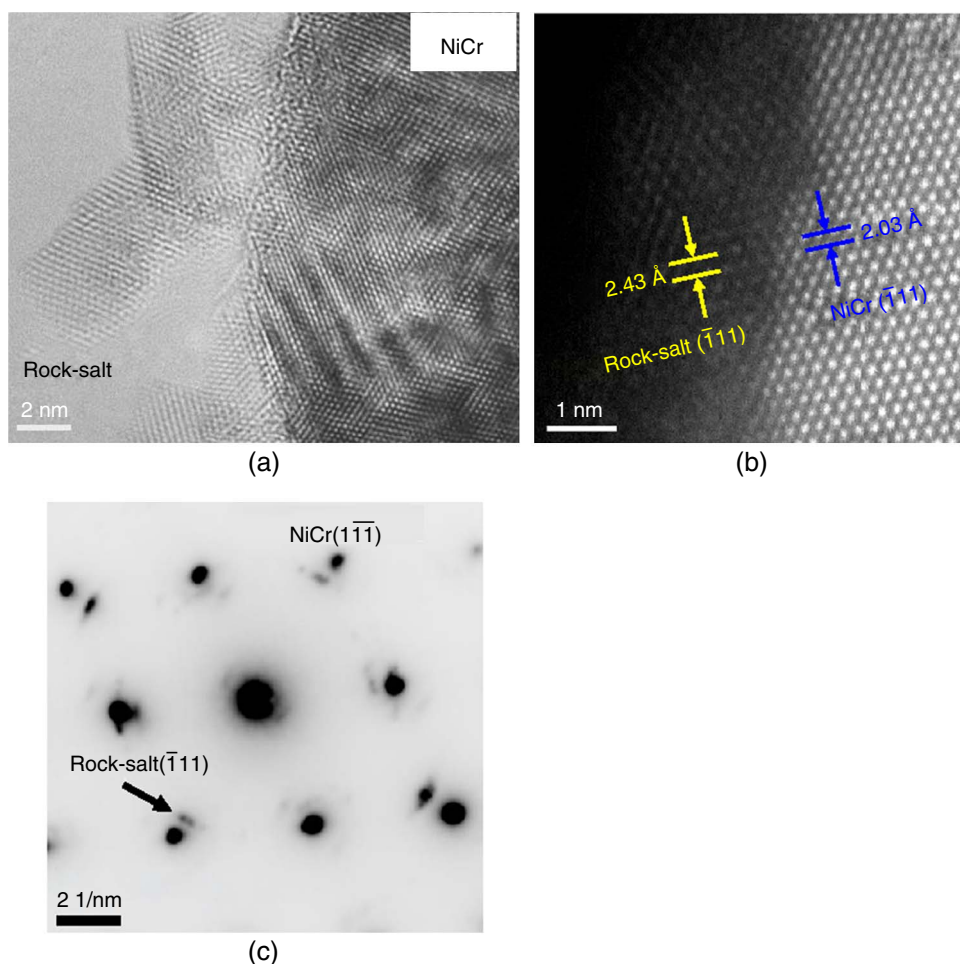


FIGURE 1. High-resolution TEM (a) and HAADF-STEM (b) images showing the rock-salt islands on Ni-Cr substrate oxidized in sodium sulfate for 10,000 s and the diffraction pattern (c) indicate the cube-cube epitaxy growth.

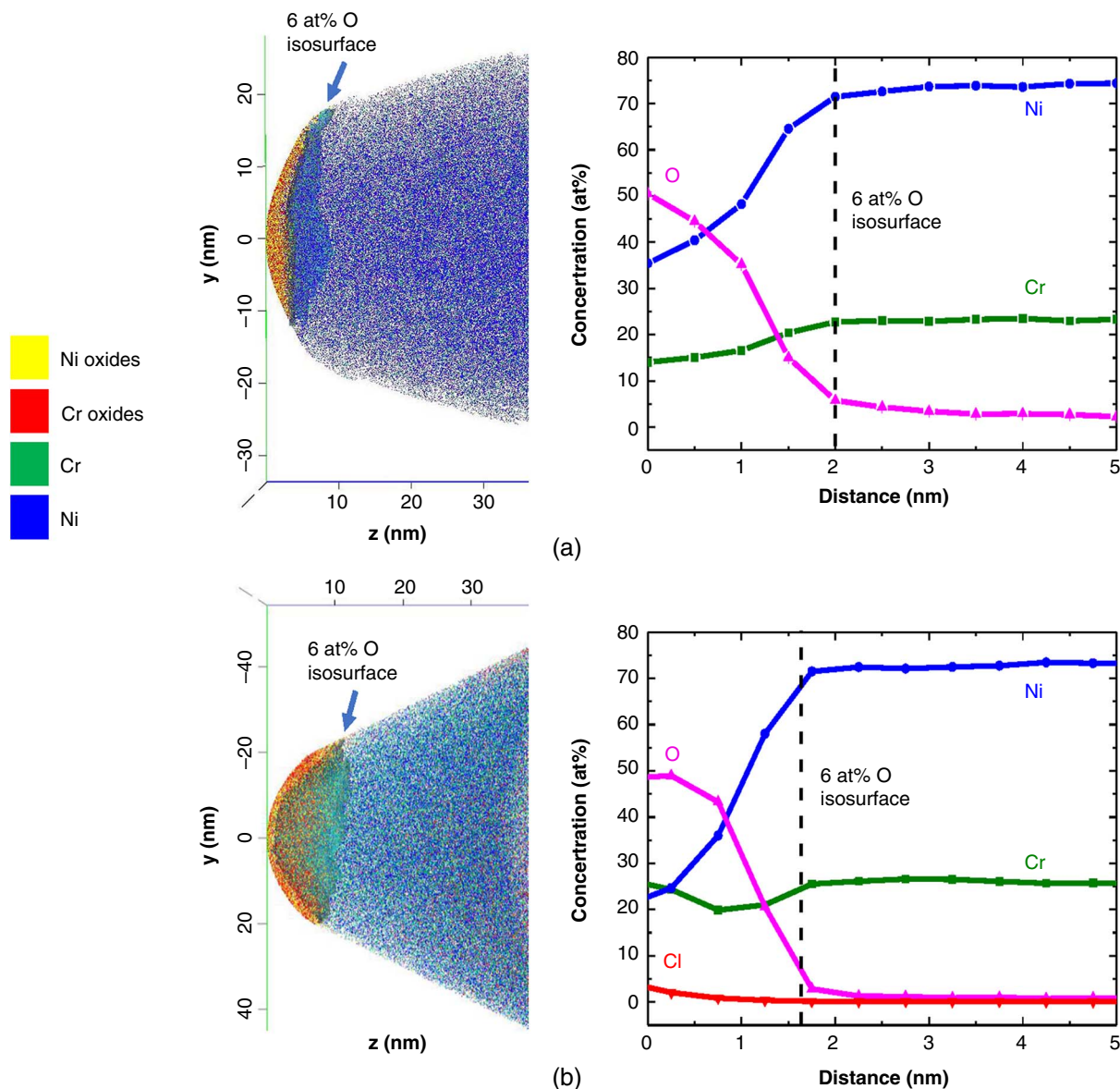


FIGURE 2. 3D APT reconstructions and proxigrams for 6 at% O isosurfaces: (a) a tip was corroded in the sodium sulfate for 10,000 s; and (b) a tip corroded in sodium chloride for 10,000 s. The oxygen concentrations were corrected using the methods mentioned in the experimental and supplementary sections.

which is consistent with the metallic state in existing database,⁴⁰ while the L_3 edge of Cr in rock-salt oxide shifts by 0.9 eV compared to that of metallic Cr. The L_3 edge of Cr^{3+} is at about 579 eV⁴⁰ in Cr_2O_3 indicating that Cr was oxidized slightly (probably Cr^{2+}), but not the Cr^{3+} in Cr_2O_3 .

3.2 | Experimental Results with Chloride

For the samples corroded in a sodium chloride containing electrolyte, high-resolution TEM and high-angle annular dark-field (HAADF) images, as well as diffraction patterns in Figures 4(a) through (c), show the oxides with corundum structure are growing out, and there is significantly less rock-salt. The corundum structure is not the “conventional” Cr_2O_3 because solute Ni atoms are also captured in corundum. The APT results in Figure 2(b) show a higher Cr content in the oxide layer. The Ni:Cr ratio of oxides is 2.3 for the corrosion in the sodium sulfate electrolyte, and decreases to less than 1 for the corrosion

in sodium chloride electrolyte. This is consistent with the dissolution of Ni^{2+} from oxide in Cl^- and possible enrichment in Cr, as suggested by Lloyd, et al.⁴¹

In Figure 2(b), the chloride concentration is high (~5 at%) at the oxide surface and decreases rapidly to moving into the oxide (about 1 nm in depth), which clearly indicates that there is chemical absorption on the surface rather than any incorporation of chlorine ion into the oxide layers. We note that the radius of chlorine ion is large, so it is difficult or impossible for chlorine ion penetrating into the bulk oxide as demonstrated by prior DFT calculations.^{42–44} However, we note that most of the local regions we checked by TEM and APT did not contain defects such as grain boundary, which may act as channels for chloride diffusing in.

A point of some importance: the oxide interface was significantly rougher when chloride was present. This is shown in Figure 5, where on the left the rock-salt for the sample without

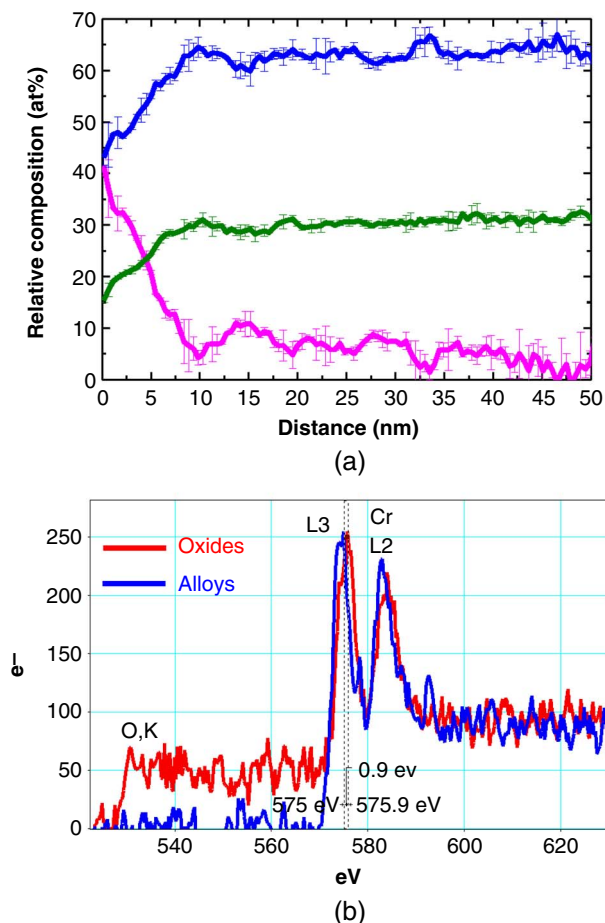


FIGURE 3. (a) Composition profile by EELS showing a large amount of Cr is captured in the rock-salt structure after oxidation in sodium sulfate. (b) L edge of Cr in rock-salt oxide shifting by 0.9 eV compared to that of metallic Cr indicating that Cr was oxidized but not the same as Cr^{3+} in Cr_2O_3 .

chloride is conformal, whereas with chloride it is rough on the scale of approximately 10 nm. This is exactly what is expected for a roughening transition due to a reduction in the surface-free energy due to inhomogeneous chemisorption,⁷ as will be discussed further in the Discussion section.

One extreme example is shown in the APT results of Figures 6 and 7. For this sample, there were clear nanometer scale, high-aspect ratio, nanopit features penetrating into the alloy. These regions are roughly 30 nm deep and 10 nm wide. Statistically, these nanopit features are probably rare, we only have one example, but as APT samples containing very small volumes we argue it is appropriate to show the rare event that we were able to capture. The APT results indicate that the nanopits contain significant concentrations of Cl^- which is consistent with the trapped liquid within them. (Note that due to the posttreatment drying the Cl^- concentration will not be fully representative of the solution during the preparation.) The penetrations are suggestive of a morphological instability in the oxide, as discussed in the Discussion section. We note that many averaged experiments (e.g., depth-profiling x-ray photoelectron spectroscopy) have implied that chloride can penetrate the oxide in some metals such as aluminum;¹⁸ nanopits containing the trapped liquid similar to those shown in Figures 6 and 7 will lead to spatial averaging depth profiling

experiments such as using x-ray photoelectron experiments yielding results that suggest chloride penetration into the oxide, although all our experimental evidence indicates that this is an incorrect interpretation at least for the alloys we have investigated.

3.3 | Density Functional Theory Results with Chloride

To elucidate the chloride effect on the NiO and Cr_2O_3 surface, the enthalpy of surface chemisorption and work function as a function of the surface coverage of chloride were calculated. We used the well-established hydroxylated 1×1 NiO (111) surface⁴⁵ as the starting point, and the similar fully hydroxylated surfaces for Cr_2O_3 (001) surfaces, as shown in Figures 8(a) and (b). We note that NiO is isostructural to MgO, and Cr_2O_3 to Al_2O_3 so all the relevant structures could be obtained by modifying the structures previously found for MgO and Al_2O_3 ⁷ with modification to include the appropriate antiferromagnetic ordering.

The results in Figure 9 are consistent with our previous calculations on the MgO (111) and Al_2O_3 (001) surfaces,⁷ with slight differences because nickel and chromium are both less electropositive. The first generalization is that in a large range of coverage the surface-free energy of hydroxylated NiO (111) is significantly reduced by chloride absorption. For Cr_2O_3 (001) surface, the hydrogen bonding networks in Figure 8(b) are also seen as for Al_2O_3 (001) surface, which has a significant contribution due to stabilization of the surface by passivating the metallic surface in an aqueous environment with chlorine.⁷ The absorption of chloride will disrupt the hydrogen bonding network, as shown in the right panel of Figure 8(b). Similar to the prior work there is also a general reduction of the work function as expected (not shown here).

The key result is that one has a significant reduction in the surface-free energy with chloride, showing large variations with the exposed surface crystallography. This connects directly to the surface roughening shown in Figure 5.

DISCUSSION

The results of TEM and APT show the details of oxide structure and composition with and without chloride-containing media. While rock-salt and corundum structures form, they have dopants such as Cr in rock-salt far in excess of the solubility limits. This is a consequence of non-equilibrium solute capture, as discussed in more detail elsewhere.³⁸

Compared to the sodium sulfate electrolyte, the rock-salt oxide thin film tends to thin, and a Cr-rich oxide with a corundum structure is formed in the chloride-containing solution. DFT calculations indicate a significant reduction of rock-salt (111) surface-free energy due to the chloride absorption, similar to MgO (111) as discussed previously.

There is also a significant reduction in the surface energy for corundum, although this depends very strongly upon the exposed surface. In the corundum structure, along the [001] direction there are alternating hexagonal planes, but only two of the possible three metal sites are occupied. The hydrogens can rotate to lie above the surface metal vacant site and bond to two oxygens. This hydrogen bonding network stabilizes the passive thin film in an aqueous environment. In contrast, corundum (100) is much more susceptible to chloride chemisorption. In both cases, chloride in solution competes with the hydroxide on the oxide surface and disrupts the hydrogen-bonded network. For an engineering alloy with many different

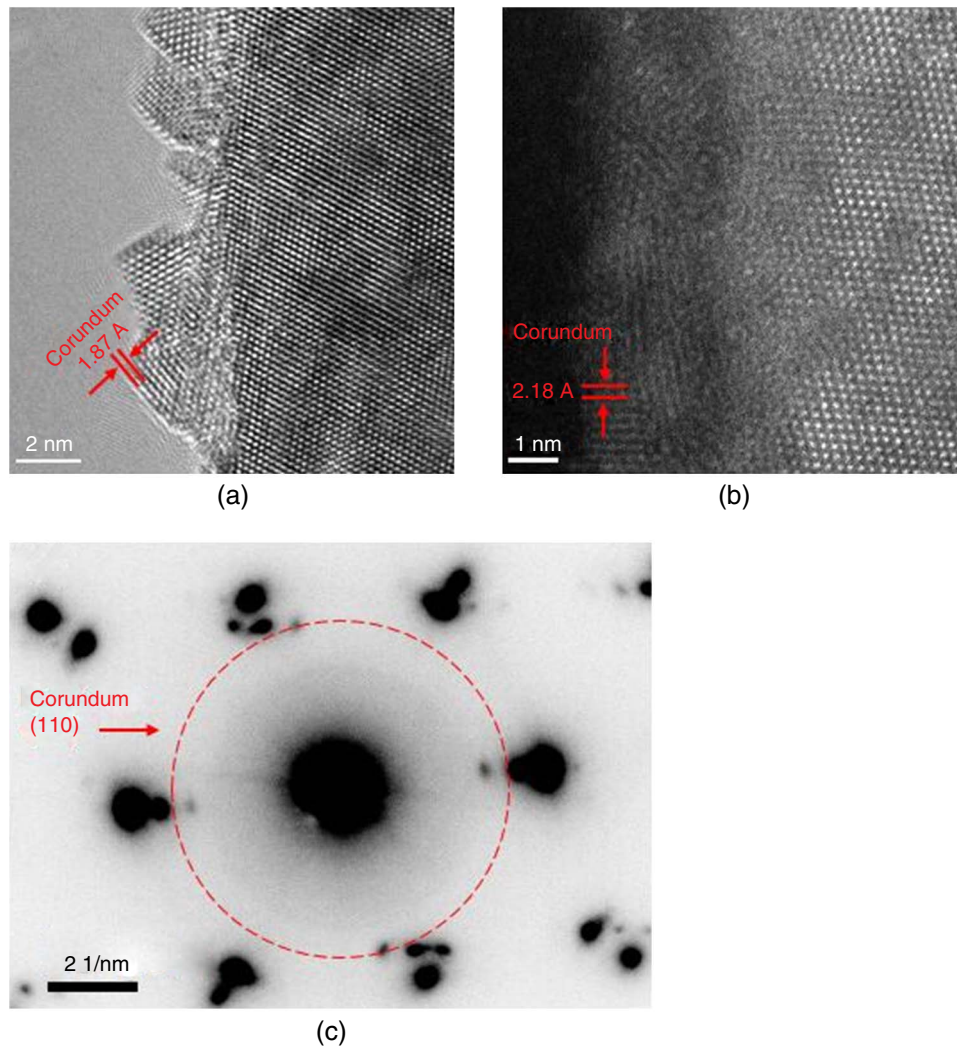


FIGURE 4. High-resolution TEM (a) and HAADF-STEM (b) images showing corundum grains on the surface of Ni-Cr oxidized in sodium chloride for 10,000 s and the diffraction pattern in (c).

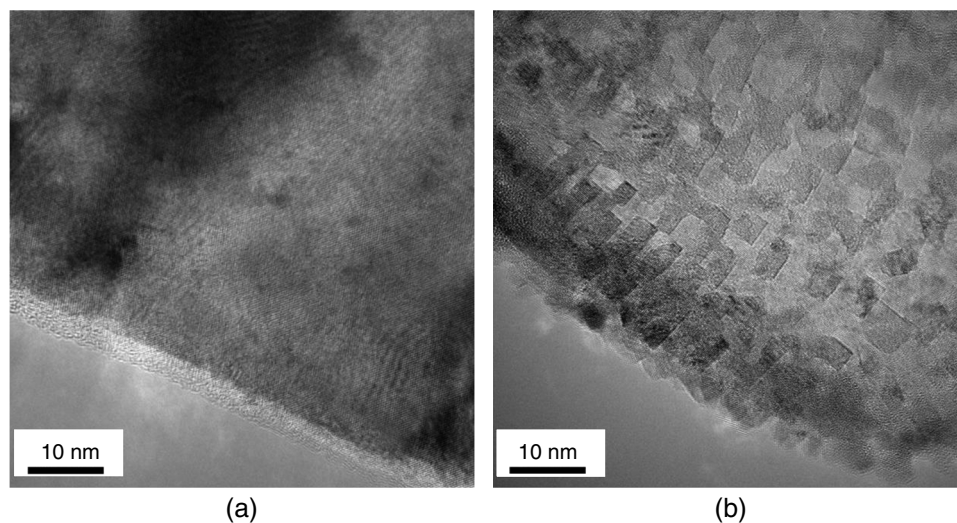


FIGURE 5. Low-magnification images of sample surface oxidized in sodium sulfate (a) and in sodium chloride (b) showing a rougher surface due to the inhomogeneous reduction in surface-free energy due to competitive chemisorption of chloride, with diffraction patterns showing the cube-cube epitaxy inset in both.

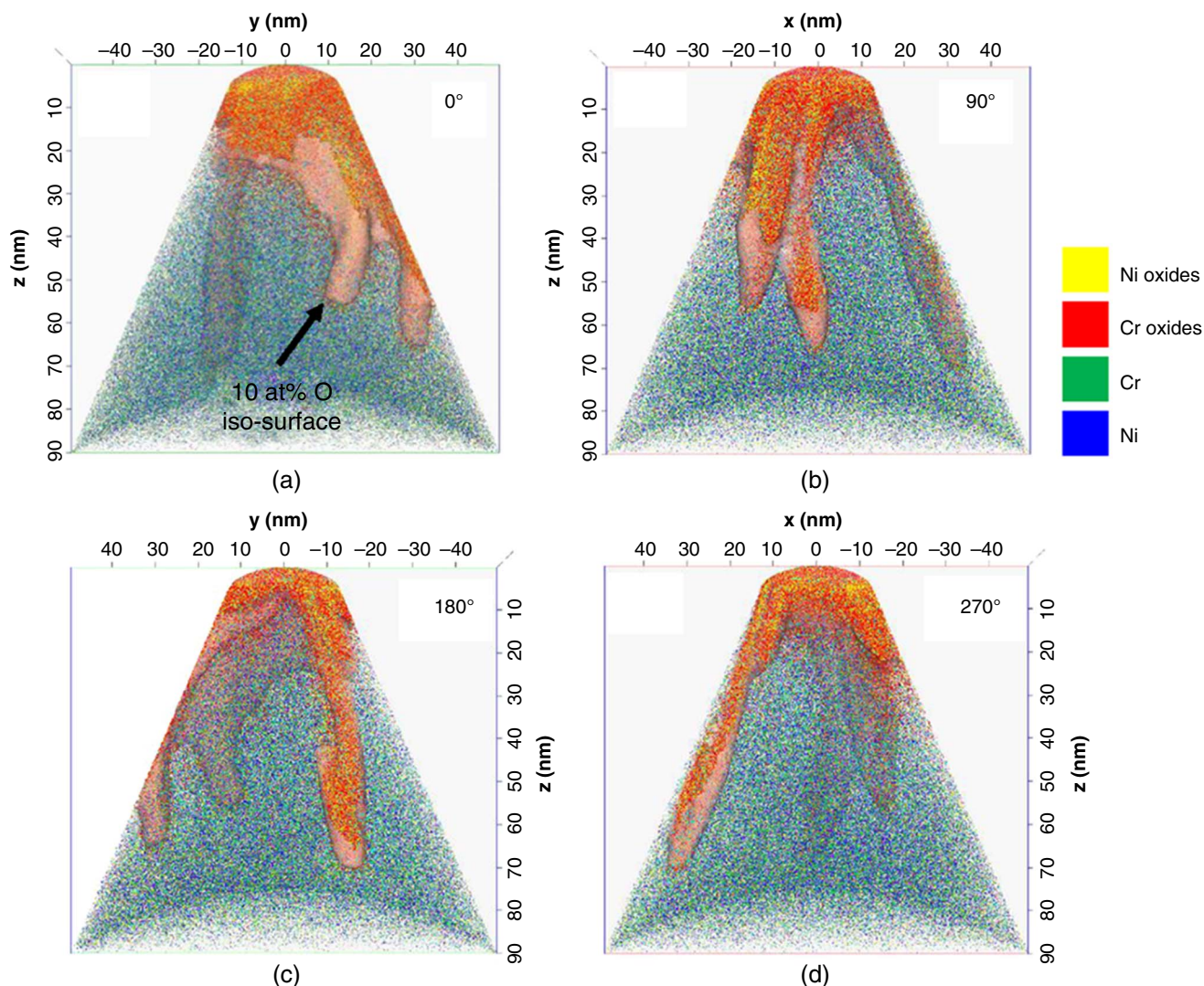


FIGURE 6. (a) through (d) APT reconstruction with 10 at% O isosurface at different rotation angles of a tip oxidized in sodium chloride shows nanometer scale features penetrating into the alloy.

oxide surface crystallography, some will be susceptible to attack, others not. (We note that for chromia the (100) hydroxylated surface is lower in free energy than (001), although both will be present on the Wulff construction shape.)

To connect these reductions in surface energy to the experimental results, some care is needed to differentiate between cause and effect. As is well documented in the literature, the presence of chloride leads to rougher surfaces, the effect. It is sometimes considered that this is purely a kinetic effect, for instance, preferential dissolution at grain boundaries. However, this is not necessarily correct. To illustrate this, Figure 10 shows the thermodynamic shape of a small oxide nanoparticle with an isotropic surface energy on a flat metal support using the conventional Winterbottom construction;⁴⁶ the shape for two particles on a metal support with a grain boundary using a Summertop construction⁴⁷ with a modified-Wulff approach⁴⁸ where the grain boundary energy is divided in half can be found in Marks.⁷ (Details about such constructions can be found in Marks and Peng⁴⁹ and references therein.) The shape of the single particle is determined by the *ratio* of the surface and interfacial-free energies which include

contributions from chemisorption. Increasing the interfacial energy (i.e., less adhesion) raises the oxide particle above the interface, as does decrease the surface-free energy due to chemisorption. Similarly, for the bicrystals, the magnitude of the grain boundary groove depends upon the *ratio* of the surface and grain boundary energies. Chloride penetration into a grain boundary thereby decreasing the adhesion between the grains will lead to an increased grooving but is not the only possible cause; chemisorption has the same effect. For completeness, we note that the chloride ion is significantly larger than the oxide ion, so the substitution of chloride for oxygen is typically quite endothermic, as demonstrated by specific DFT calculations.⁴²⁻⁴⁴

The previous example refers to the thermodynamic shapes. To convert to kinetic shapes, i.e., kinetic Wulff variants (e.g., Marks and Peng⁴⁹ and references therein) the surface energies are replaced by dissolution velocities and the origin for Wulff constructions is in the fluid in some cases. Similar to the thermodynamic case there are ambiguities about cause and effect. Treating dissolution in a standard fashion as the inverse of conventional step-flow crystal growth, the chemical potential

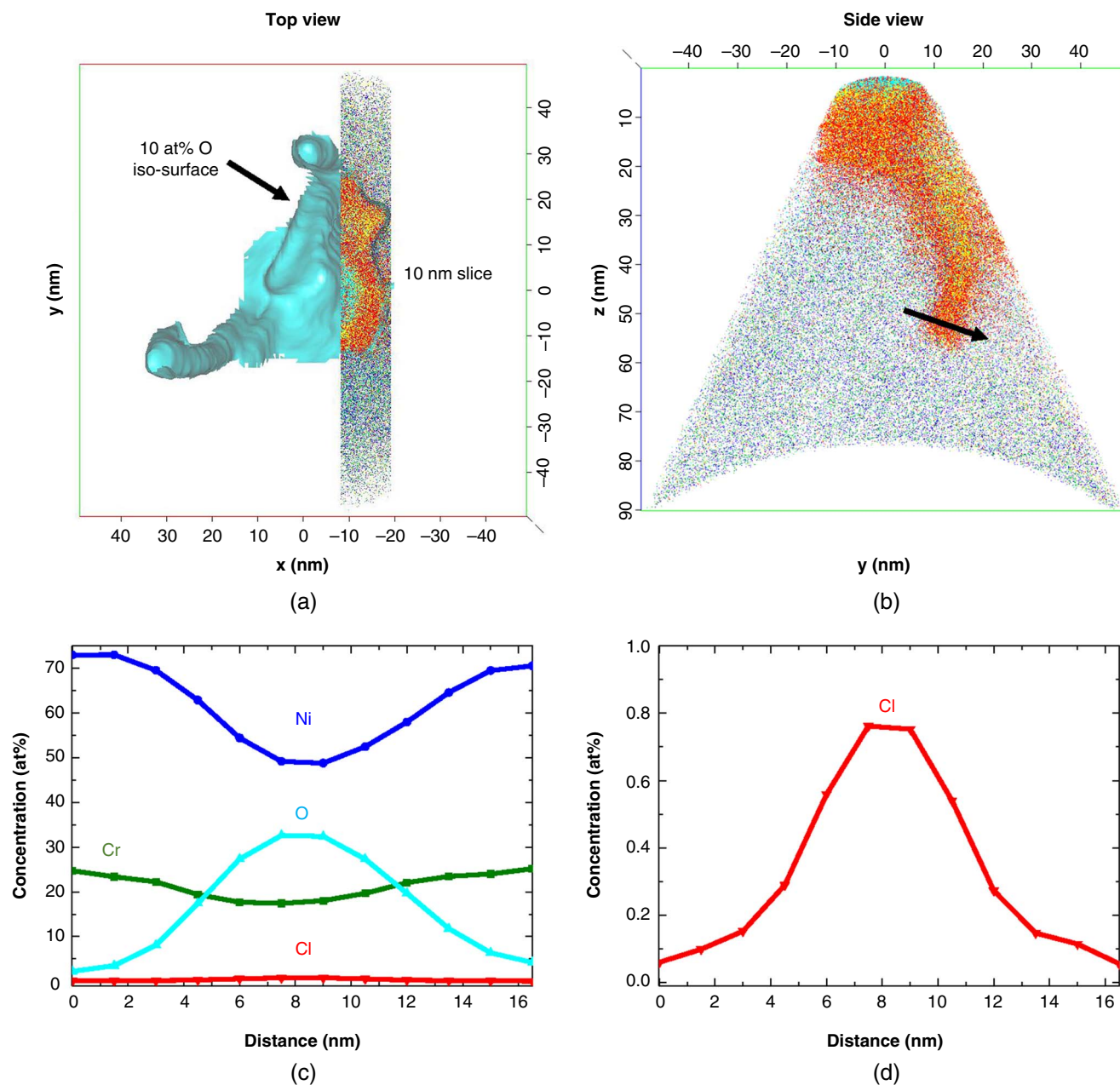


FIGURE 7. (a) Top and side view (b) of the nanoscale features by APT, reconstruction in (c) and (d) the 1D composition profile across them which shows enrichment of O and Cl.

change per atom for dissolution of a circular terrace of radius R on a flat surface can be written as

$$\Delta\mu = \Delta\mu_0 + \gamma_{\text{Step}}\Omega/R \quad (1)$$

where $\Delta\mu_0$ is the difference between the bulk chemical potential per atom in the bulk and solution including dependencies such as pH and cation chelation, γ_{Step} is the step energy per unit length, and Ω the relevant atomic volume. A grain boundary can be treated similar to a twin boundary in a modified kinetic Wulff construction⁵⁰ by adding an enhancement term for dissolution because of the addition energy of the grain boundary. The chemical potential for dissolution at a grain boundary creates

new surface (assuming an existing groove) and can similarly be written as

$$\Delta\mu = \Delta\mu_0 - \gamma_{\text{Gb}}\Omega/h_{\text{gb}} + 2\gamma_{\text{Surf}}\Omega/Rh_{\text{Surf}} \quad (2)$$

where h_{gb} and h_{Surf} are effective interatomic distances for the grain boundary and step. (Rigorously this should be treated using a weighted mean curvature for the grain boundary) Reducing the steps energy, as shown in specific DFT calculations,⁵¹ will increase dissolution of the surface but there will also be a larger increase in the driver for dissolution at the grain boundary, leading to apparent faster dissolution at the grain boundary.

Hence, the reduction in surface and/or step energies due to chloride chemisorption for both thermodynamic and kinetic

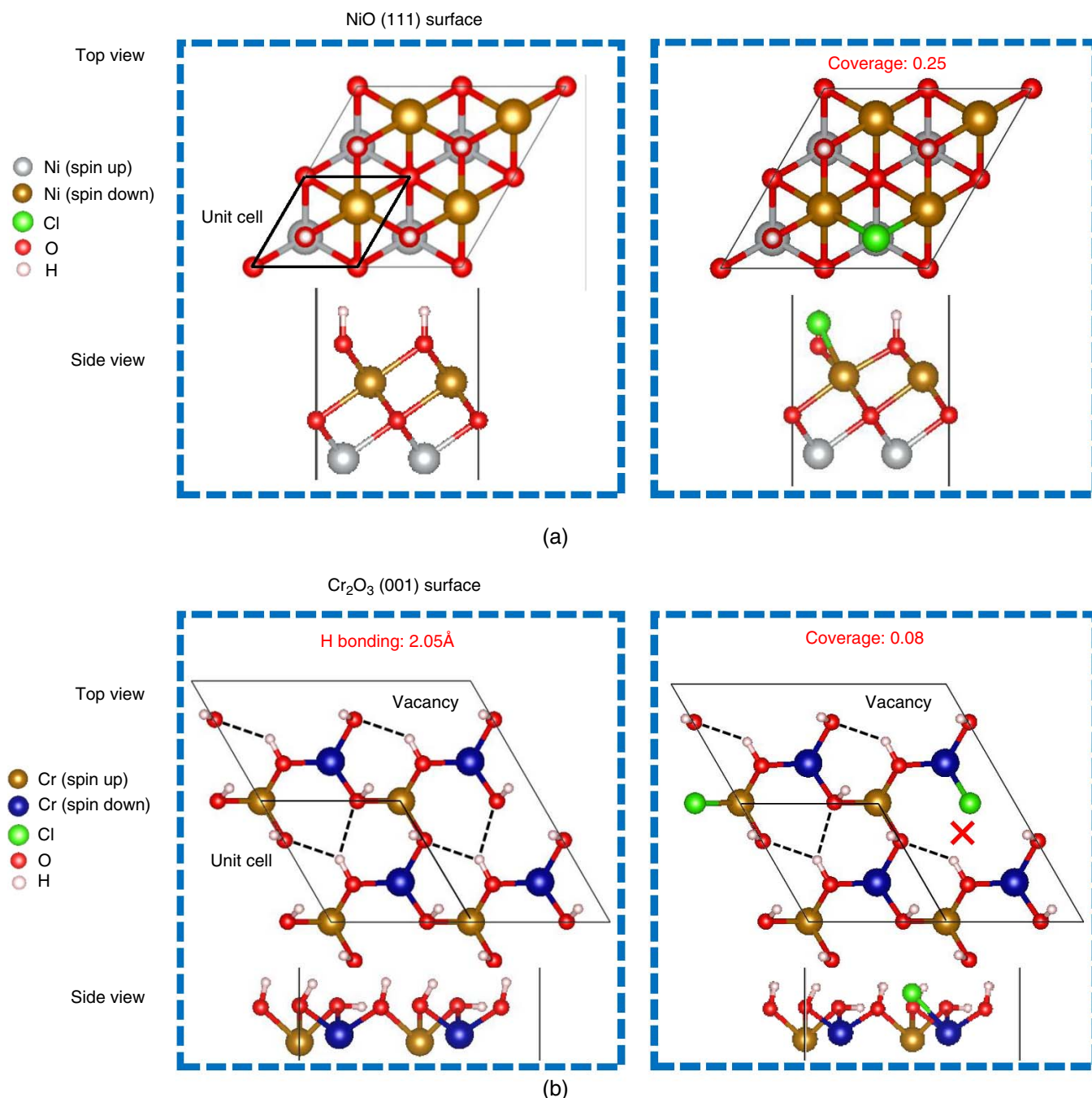


FIGURE 8. (a) Structures on the NiO (111) surface used for the DFT, on the left the 1×1 hydroxylated surface viewed from the top and side, with the surface unit cell indicated and on the right the chloride surface where some of the hydroxides have been replaced by chloride. (b) Structures on the Cr₂O₃ (001) surface, on the left the 1×1 hydroxylated surface viewed from the top and side, with the surface unit cell indicated and on the right the 0.08 coverage chloride. The dash lines indicate the hydrogen bonds.

control has the apparent effect of increasing etching at grain boundaries and appears to decrease the adhesion to the substrate and roughen surfaces. This will lead to a dewetting of the oxide which is apparent in the experimental data, for instance, Figure 5.

It is useful to expand a little more and connect this to a morphological instability approach, which describes the evolution of a film. Roughening and breakdown of the oxide film depend upon the competition between two competing free

energy drivers; see Marks⁷ and references therein for more details. Starting with a planar oxide, a small perturbation (e.g., a Fourier modulation of the oxide thickness) can either grow with time or decay, in both cases exponentially. Being specific, one considers a perturbation in the oxide thickness h , of

$$h(x,y,t) = h_0 \exp(\sigma(k)t) \exp(ikx) \quad (3)$$

where x is along the surface, y is normal to it, t is time, σ is the growth rate, and k is the wavevector of the instability. If $\sigma > 0$,

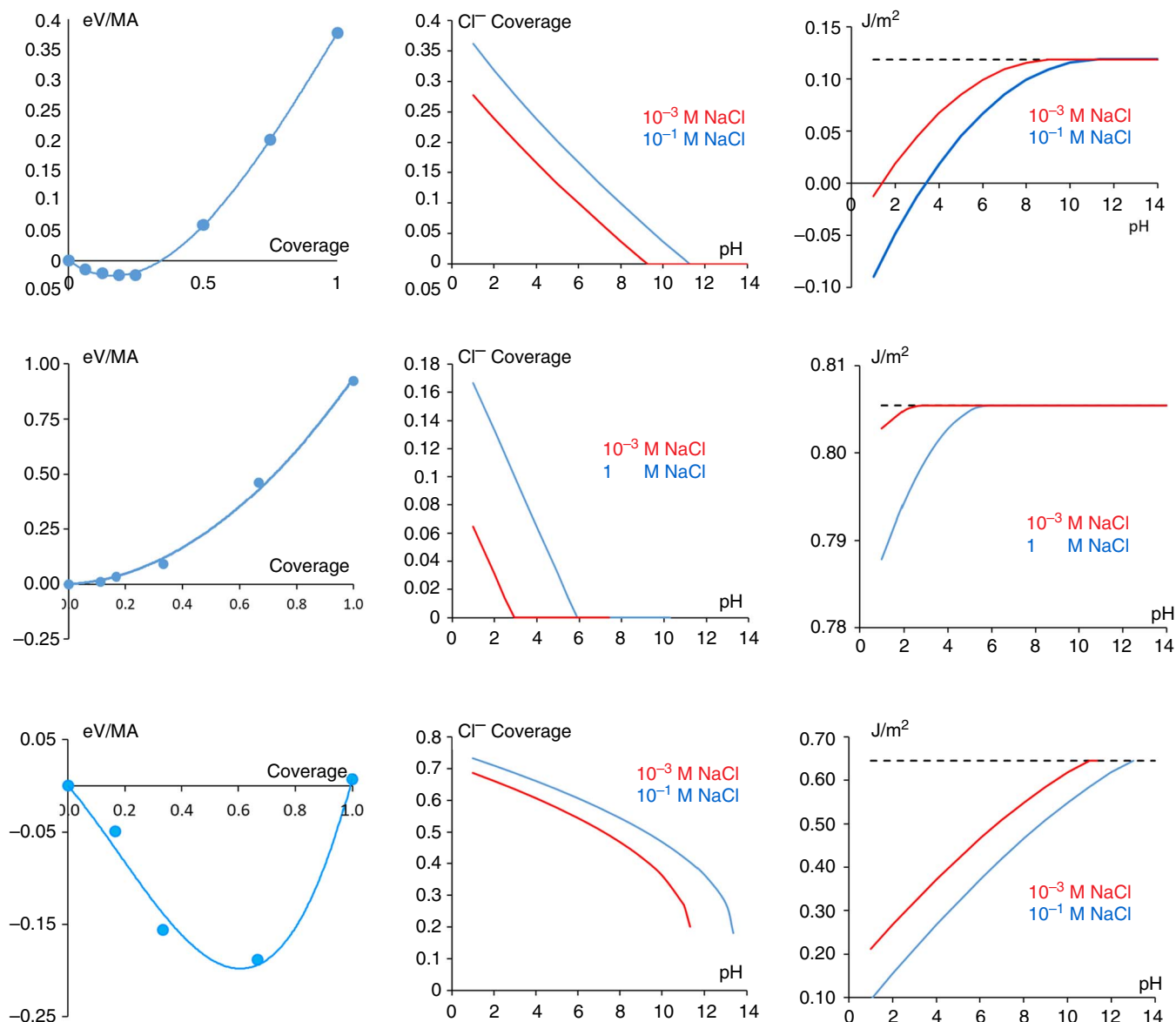


FIGURE 9. Composite of, on the left, the enthalpy of chloride chemisorption vs. coverage; middle, the chloride chemisorption vs. pH for two chloride molarities; and on the right the surface free energy. From top to bottom are shown NiO (111), Cr₂O₃ (001), and Cr₂O₃ (100).

the instability will grow exponentially. The general form of the growth rate is:

$$\sigma(k) = M(Ak^{n-1} - \gamma k^n) \quad (4)$$

where the order n depends upon the nature of the destabilizing driver, M and A are constants, and γ is the surface-free energy. For growth dissolution, $n = 2$; for surface diffusion, $n = 4$; and for bulk diffusion, $n = 3$. This leads to a rate which is given by the maximum value σ_{\max} and wavevector k_{\max}

$$\sigma_{\max} \sim MA^n / \gamma^{n-1}; \quad k_{\max} \sim A / \gamma \quad (5)$$

To illustrate this, Figure 11 (reproduced with permission from Spencer and Meiron⁵²) shows the evolution with time of instability. In principle, the instability can grow and penetrate the oxide completely leaving exposed metal. For the specific conditions of Figure 5(b), $k_{\max} \sim 8 \text{ nm}^{-1}$, which is also

approximately consistent with the width of the trenches in Figures 6 and 7. This strongly implies that the surface oxide roughening process and the nanopit in the metal are connected.

Note that stabilizing the surface by reducing the surface energy may appear to be inconsistent with the documented increase in dissolution rate in chloride. However, the oxide dissolution rate is what would be used in an effective medium approximation⁵³⁻⁶⁶ 1D transport model similar to those already in the literature.⁶⁷⁻⁸¹ The oxide dissolution rate is a mean-field linearization that includes the increased surface area of a roughened oxide film covered surface and also the spatial and temporal average over local breakdown processes.

For completeness, while it is tempting to make a connection between these nanopits, for instance, to consider them as the initial stages of pit formation, which would be too strong a statement based upon our experimental evidence—the nanopits in Figures 6 and 7 were rare events. We cannot confirm or deny that these are the initial stages of pitting. While a morphological

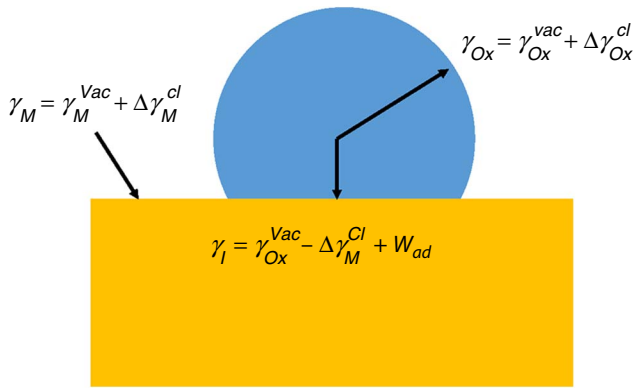


FIGURE 10. The Winterbottom shape for a single oxide nanoparticle (blue) on a substrate (orange) which depends upon the ratio of the oxide surface energy γ_{Ox} and the interfacial energy γ_i , where γ_M^{vac} and γ_{Ox}^{vac} are the surface energies in vacuum of the metal and oxide, respectively, $\Delta\gamma_M^{cl}$ and $\Delta\gamma_{Ox}^{cl}$ the change in surface energies due to chemisorption of chloride (or hydroxide) and W_{ad} the energy per unit area released when the two vacuum surfaces are joined. The apparent wetting and (not shown) the size of the grain boundary groove depends upon the ratios of energies, so reducing chemisorption leads to apparent decohesion and grain boundary etching.

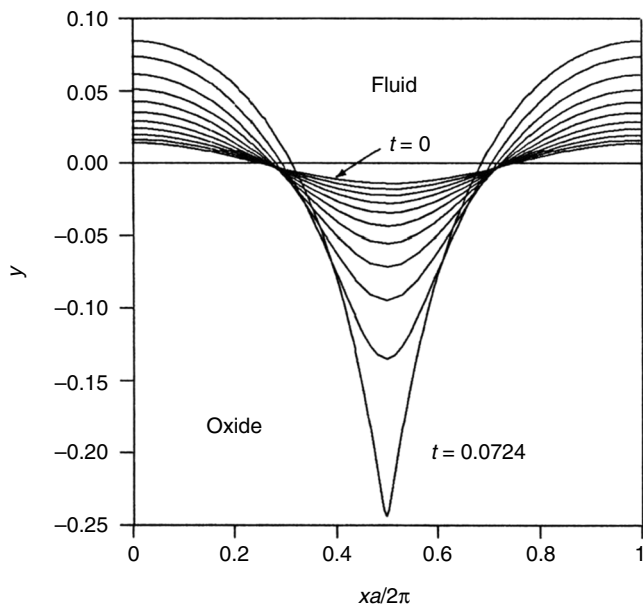


FIGURE 11. Time-dependent evolution of a morphological instability, reproduced with permission from Spencer and Merion.⁵² The regions marked "Fluid" and "Oxide" have been added to the figure to represent the experiments herein.

instability in the oxide as described previously can technically continue to grow into the metal, this neglects other effects. During the process, there may be depletion of the chloride in the pit which may cause repassivation when the mass transport rate out of the pit exceeds the metal cation generation rate into the pit or when the potential driving force is reduced by ohmic potential drop or other processes.

In addition, there are likely to be structural variations in the metal, for instance, internal grain boundaries or fluctuations in the local alloy composition which will change the growth

rate. Pure exponential dissolution is almost certainly an oversimplification, and a much more likely process is conventional stick-slip, i.e., dissolution spurts. While it is certainly plausible that in some cases these can grow large enough that a larger scale pit develops as the side walls start to dissolve, we cannot confirm or deny that this takes place. Ideal experiments would involve direct in situ observations using electron microscopy which are at the frontier of what can currently be done because of current technical limitations such as resolution degradation due to windows and liquid scattering; we leave this to future work.

In summary, the experimental results are consistent with expectations based upon density functional modeling and strongly imply that the role of chloride is via preferential adsorption on some oxide surfaces, not others, leading to inhomogeneous reductions of the surface energy, roughening and morphological instabilities in the oxide film which can expose bare metal. At this point, conventional pit stabilization theories may apply.

ACKNOWLEDGMENTS

The author acknowledges support from ONR MURI "Understanding Atomic Scale Structure in Four Dimensions to Design and Control Corrosion Resistant Alloys" on Grant Number N00014-16-1-2280. The authors would like to thank Peter Voorhees for useful discussions.

References

1. D.D. Macdonald, *Pure Appl. Chem.* 71, 6 (1999): p. 951-978.
2. Z. Szklarska-Smialowska, *Corros. Sci.* 41, 9 (1999): p. 1743-1767.
3. P.M. Natishan, W.E. O'Grady, *J. Electrochem. Soc.* 161, 9 (2014): p. C421-C432.
4. J. Soltis, *Corros. Sci.* 90 (2015): p. 5-22.
5. D. Arnott, N. Ryan, B. Hinton, B. Sexton, A. Hughes, *Appl. Surf. Sci.* 22 (1985): p. 236-251.
6. Y.-S. Choi, J.-G. Kim, *Corrosion* 56, 12 (2000): p. 1202-1210.
7. L. Marks, *Corrosion* 74, 3 (2018): p. 295-311.
8. T.P. Hoar, *Corros. Sci.* 7, 6 (1967): p. 341-355.
9. N. Sato, *Electrochim. Acta* 16, 10 (1971): p. 1683-1692.
10. Y. Xu, *J. Electrochem. Soc.* 140, 12 (1993): p. 3448-3457.
11. H.H. Strehblow, *Mater. Corros./Werkst. Korros.* 27, 11 (1976): p. 792-799.
12. H.H. Strehblow, B. Titze, *Corros. Sci.* 17, 6 (1977): p. 461-472.
13. H.H. Strehblow, *Werkst. Korros.* 35, 10 (1984): p. 437-448.
14. B. Macdougall, M. Cohen, *J. Electrochem. Soc.* 124, 8 (1977): p. 1185-1190.
15. W. Khalil, S. Haupt, H.H. Strehblow, *Werkst. Korros.* 36, 1 (1985): p. 16-21.
16. F. Di Quarto, *J. Electrochem. Soc.* 131, 12 (1984): p. 2901.
17. S.P. Mattin, G.T. Burstein, *Phil. Mag. Lett.* 76, 5 (1997): p. 341-347.
18. S.Y. Yu, W.E. O'Grady, D.E. Ramaker, P.M. Natishan, *J. Electrochem. Soc.* 147, 8 (2000): p. 2952-2958.
19. T.P. Hoar, D.C. Mears, G.P. Rothwell, *Corros. Sci.* 5, 4 (1965): p. 279-289.
20. P. Marcus, V. Maurice, H.H. Strehblow, *Corros. Sci.* 50, 9 (2008): p. 2698-2704.
21. R. Kirchhofer, M.C. Teague, B.P. Gorman, *J. Nucl. Mater.* 436, 1-3 (2013): p. 23-28.
22. A. Devaraj, R. Colby, W.P. Hess, D.E. Perea, S. Thevuthasan, *J. Phys. Chem. Lett.* 4, 6 (2013): p. 993-998.
23. D. Santhanagopalan, D.K. Schreiber, D.E. Perea, R.L. Martens, Y. Janssen, P. Khalifah, Y.S. Meng, *Ultramicroscopy* 148 (2015): p. 57-66.
24. G. Kresse, J. Hafner, *Phys. Rev. B: Condens. Matter* 47, 1 (1993): p. 558-561.
25. G. Kresse, J. Furthmuller, *Phys. Rev. B* 54, 16 (1996): p. 11169-11186.
26. G. Kresse, D. Joubert, *Phys. Rev. B* 59, 3 (1999): p. 1758-1775.

27. P. Blaha, K. Schwarz, G.K.H. Madsen, D. Kvasnicka, J. Luitz, R. Laskowski, F. Tran, L.D. Marks, *An Augmented Plane Wave + Local Orbitals Program for Calculating Crystal Properties* (Wien, Austria: Technische Universitat, 2018).
28. P.E. Blochl, *Phys. Rev. B: Condens. Matter* 50, 24 (1994): p. 17953-17979.
29. J.P. Perdew, K. Burke, M. Ernzerhof, *Phys. Rev. Lett.* 77, 18 (1996): p. 3865-3868.
30. S.L. Dudarev, G.A. Botton, S.Y. Savrasov, C.J. Humphreys, A.P. Sutton, *Phys. Rev. B* 57, 3 (1998): p. 1505-1509.
31. A. Rohrbach, J. Hafner, G. Kresse, *Phys. Rev. B* 69, 7 (2004): p. 075413.
32. H.J. Monkhorst, J.D. Pack, *Phys. Rev. B* 13, 12 (1976): p. 5188-5192.
33. P. Novak, J. Kunes, L. Chaput, W.E. Pickett, *Phys. Status Solidi B* 243, 3 (2006): p. 563-572.
34. F. Tran, P. Blaha, K. Schwarz, P. Novak, *Phys. Rev. B* 74, 15 (2006): p. 155108.
35. F. Tran, J. Kunes, P. Novak, P. Blaha, L.D. Marks, K. Schwarz, *Comput. Phys. Commun.* 179, 11 (2008): p. 784-790.
36. J. Sun, A. Ruzsinszky, J.P. Perdew, *Phys. Rev. Lett.* 115, 3 (2015): p. 036402.
37. L.D. Marks, *J. Chem. Theory Comput.* 9, 6 (2013): p. 2786-2800.
38. X.X. Yu, A. Gulec, Q. Sherman, K.L. Cwalina, J.R. Scully, J.H. Perepezko, P.W. Voorhees, L.D. Marks, *Phys. Rev. Lett.* 121 (2018): p. 145701.
39. C.H. Chen, M.R. Notis, D.B. Williams, *J. Am. Ceram. Soc.* 66, 8 (1983): p. 566-571.
40. T.L. Daulton, B.J. Little, *Ultramicroscopy* 106, 7 (2006): p. 561-573.
41. A.C. Lloyd, J.J. Noel, S. McIntyre, D.W. Shoesmith, *Electrochim. Acta* 49, 17-18 (2004): p. 3015-3027.
42. N. Pineau, C. Minot, V. Maurice, P. Marcus, *Electrochim. Solid. St.* 6, 11 (2003): p. B47-B51.
43. A. Bouzoubaa, B. Diawara, V. Maurice, C. Minot, P. Marcus, *Corros. Sci.* 51, 4 (2009): p. 941-948.
44. A. Bouzoubaa, D. Costa, B. Diawara, N. Audiffren, P. Marcus, *Corros. Sci.* 52, 8 (2010): p. 2643-2652.
45. F. Rohr, K. Wirth, J. Libuda, D. Cappus, M. Bäumer, H.-J. Freund, *Surf. Sci.* 315, 1-2 (1994): p. L977-L982.
46. W.L. Winterbottom, *Acta Metall. Mater.* 15, 2 (1967): p. 303-310.
47. R.K.P. Zia, J.E. Avron, J.E. Taylor, *J. Stat. Phys.* 50, 3-4 (1988): p. 727-736.
48. L.D. Marks, *J. Cryst. Growth* 61, 3 (1983): p. 556-566.
49. L.D. Marks, L. Peng, *J. Phys. Condens. Matter* 28, 5 (2016): p. 053001.
50. E. Ringe, R.P. Van Duyne, L.D. Marks, *J. Phys. Chem. C* 117, 31 (2013): p. 15859-15870.
51. A. Bouzoubaa, B. Diawara, V. Maurice, C. Minot, P. Marcus, *Corros. Sci.* 51, 9 (2009): p. 2174-2182.
52. B.J. Spencer, D.I. Meiron, *Acta Metall. Mater.* 42 (1994): p. 3629-3641.
53. D.A.G. Bruggeman, *Ann. Phys.-Berlin* 24, 7 (1935): p. 636-664.
54. D.J. Bergman, *Phys. Rep.* 43, 9 (1978): p. 378-407.
55. R.I. Cukier, *J. Phys. Chem.* 89, 2 (1985): p. 246-252.
56. X.C. Zeng, D.J. Bergman, P.M. Hui, D. Stroud, *Phys. Rev. B: Condens. Matter* 38, 15 (1988): p. 10970-10973.
57. C. David, Y. Gueguen, G. Pampoukis, *J. Geophys. Res.-Solid* 95, B5 (1990): p. 6993-7005.
58. C.W. Nan, *Prog. Mater. Sci.* 37, 1 (1993): p. 1-116.
59. P.M. Hui, P. Cheung, Y.R. Kwong, *Physica A* 241, 1-2 (1997): p. 301-309.
60. P.P. Castañeda, P. Suquet, in *Advances in Applied Mechanics*, vol. 34 (Amsterdam, The Netherlands: Elsevier, 1997), p. 171-302.
61. D. Stroud, *Superlattice Microst.* 23, 3-4 (1998): p. 567-573.
62. D.J. Bergman, D.G. Stroud, in *Response of Composite Media Made of Weakly Nonlinear Constituents*, ed. V.M. Shalaev, vol. 82 (Berlin, Germany: Springer, 2002), p. 19-39.
63. F. Willot, Y.P. Pellegrini, P.P. Castaneda, *J. Mech. Phys. Solids* 56, 4 (2008): p. 1245-1268.
64. M.I. Idiart, F. Willot, Y.P. Pellegrini, P.P. Castaneda, *Int. J. Solids Struct.* 46, 18-19 (2009): p. 3365-3382.
65. A.J. Haija, W.L. Freeman, R. Umbel, *Physica B* 406, 22 (2011): p. 4266-4271.
66. L. Li, S. Holland, *NanoMater. Energy* 3, 4 (2014): p. 139-147.
67. C. Wagner, *Z. Phys. Chem.* 21, 1 (1933): p. 25-41.
68. N.F. Mott, *Trans. Faraday Soc.* 35, 3 (1940): p. 0472-0482.
69. N.F. Mott, *Trans. Faraday Soc.* 43 (1947): p. 429-434.
70. N. Cabrera, N.F. Mott, *Rep. Prog. Phys.* 12 (1948): p. 163-184.
71. C.Y. Chao, *J. Electrochem. Soc.* 128, 6 (1981): p. 1187-1194.
72. L.F. Lin, C.Y. Chao, D.D. Macdonald, *J. Electrochem. Soc.* 128, 6 (1981): p. 1194-1198.
73. D.D. Macdonald, *J. Electrochem. Soc.* 139, 12 (1992): p. 3434-3449.
74. D.D. Macdonald, *Electrochim. Acta* 56, 4 (2011): p. 1761-1772.
75. M. Bojinov, G. Fabricius, T. Laitinen, K. Makela, T. Saario, G. Sundholm, *Electrochim. Acta* 45, 13 (2000): p. 2029-2048.
76. K. Leistner, C. Toulemonde, B. Diawara, A. Seyeux, P. Marcus, *J. Electrochem. Soc.* 160, 6 (2013): p. C197-C205.
77. A. Seyeux, V. Maurice, P. Marcus, *J. Electrochem. Soc.* 160, 6 (2013): p. C189-C196.
78. C. Bataillon, F. Bouchon, C. Chainais-Hillairet, C. Desgranges, E. Hoarau, F. Martin, S. Perrin, M. Tupin, J. Talandier, *Electrochim. Acta* 55, 15 (2010): p. 4451-4467.
79. C. Chainais-Hillairet, C. Bataillon, *Numer. Math.* 110, 1 (2008): p. 1-25.
80. A. Couet, A.T. Motta, A. Ambard, *Corros. Sci.* 100 (2015): p. 73-84.
81. M. Momeni, J.C. Wren, *Faraday Discuss.* 180 (2015): p. 113-135.